

Article

Establishment, Validation, and Application of a Comprehensive Thermal Hydraulic Model for a Parabolic Trough Solar Field

Linrui Ma ^{1,2,3,4}, Zhifeng Wang ^{1,2,4,*}, Dongqiang Lei ^{1,2,4} and Li Xu ^{1,2,4}

¹ Key Laboratory of Solar Thermal Energy and Photovoltaic System, Chinese Academy of Sciences, Beijing 100190, China

² Institute of Electrical Engineering, Chinese Academy of Sciences, Beijing 100190, China

³ Institute of Electrical Engineering, University of Chinese Academy of Sciences, Beijing 100049, China

⁴ Beijing Engineering Research Center of Solar Thermal Power, Beijing 100190, China

* Correspondence: zhifeng@vip.sina.com; Tel.: +86-137-0132-7862

Received: date; Accepted: date; Published: 16 August 2019

Abstract: To better understand the thermal hydraulic characteristics of the parabolic trough solar field (PTSF), a comprehensive thermal hydraulic model (CTHM) based on a pilot plant is developed in this paper. All of the main components and thermal and hydraulic transients are considered in the CTHM, and the input parameters of the model are no longer dependent on the total flow rate. In this paper, we solve the CTHM by a novel numerical approach based on graph theory and the Newton-Raphson method, and then examine it by two tests conducted based on a pilot plant. Comparing the flow rate, temperature, and pressure drop results show good agreement and further validate the availability and accuracy of the CTHM under hydraulic and thermal disturbance. Besides, two applications of the CTHM are implemented for presenting its potential function. In the first application, two cases are simulated to reveal how the thermal effects influence the PTSF behavior, and in the second application, the CHTF is used for the study of control strategies under uniform and nonuniform solar irradiance. The results verify the feasibility of controlling the PTSF outlet temperature through the header and loop valves.

Keywords: parabolic trough solar field; thermal and hydraulic model; validation; control

1. Introduction

Through long-time operation experience accumulation and continuous research, the parabolic trough solar thermal power plant (PTSTPP) is considered as the ripest in technique and most commercialized concentrating solar power technology [1]. The parabolic trough solar field (PTSF), where solar energy is collected and converted to the thermal energy, is the component most worth exploring in a PTSTPP [2]. In a representative PTSF, the heat transfer fluid (HTF) is distributed by the cold header and harvested by the hot header. Several parallel loops connect the cold and hot headers; each loop consists of a series of parabolic trough collectors (PTC), and the cold HTF is heated to a high temperature as it flows through the PTC loop. Finally, the hot HTF is pumped into the power block to produce the steam. As the solar irradiance and thermal requirement change, three parameters are used to adjust the flow rate of the HTF to meet the outlet temperature demand: the opening of the control valve in headers, the opening of the control valve in PTC loops, and the pump frequency [3].

The majority of the published studies that research the PTSF place emphasis on a thermal perspective. Forristall et al. [4] developed a detailed thermal steady-state model of the PTC, which is validated by the test results of a SEGS LS-2 solar collector [5]. Stuetzle et al. [6] built a thermal dynamic model of the PTC to study the control algorithm of a plant, and their measured data

validated this model. Camacho et al. [7] developed a simplified thermal dynamic model of the PTC, in which both the heat loss and heat convective coefficient are fitted as polynomials in the temperature. Padilla et al. [8] and Hachicha et al. [9] improved the thermal model in two ways: implementing a more comprehensive radiative analysis and considering that the solar flux distribution around the receiver is nonuniform, respectively. Yilmaz et al. [10] developed a comprehensive thermo-mathematical model, whose detailed optical and thermal analysis in this model allow the model to simulate more accurate results for the optical loss, heat loss, and thermal efficiency. Behar et al. [11] improved on the accuracy of thermal performance prediction of the PTC in another way, i.e., developing a novel model that can consider the flow rate variation by adapting an optimization procedure of the HTF outlet temperature.

In effect, in a large-scaled PTSF, because the flow rate in the individual PTC loop is unknown and determined by the layout, pump head, and flow resistance, a detailed thermal model of the PTC is insufficient to understand the performance of the PTSF comprehensively. Therefore, in some studies, the PTSF is regarded as a complex piping network, whose thermal hydraulic characteristics are researched. The symmetrical and uniform flow distribution of the PTSF was assumed to simulate the PTSTPP in the System Advisor Model (SAM), which was developed by the National Renewable Energy Laboratory (NREL) and Sandia National Laboratory [12]. Abutayeh et al. [13] spelled out the presence of unbalanced flow distribution in the PTSF and proposed a method to amend it. Giotri [3] studied the behavior of the PTSF under a variety of thermal transients based on a thermal hydraulic model, which contained a thermal dynamic part and a hydraulic steady pipe network part. A virtual solar field (VSF), which was developed by the German Aerospace Centre (DLR) [14], applied a thermal hydraulic model similar to [3] to simulate the behavior of the whole PTSF, and the operating data from Andasol-3 validated the model. Ma et al. [15] revealed the relationship between the flow distribution and flow resistance of the PTSF, and then verified the method proposed in [13] based on a thermal hydraulic dynamic model (THDM) and tested data obtained from a pilot plant.

Two aspects need to be improved in the existing thermal hydraulic models of the PTSF, i.e., the lack of pump module and the unaccounted hydraulic transients. The former leads to the dependence on the inlet header flow rate in simulation and validation, and the latter obscures the PTSF specific behavior under the thermal and hydraulic transients. There are two reasons for the difficulty of solving these problems by directly employing the transient hydraulic model in the water distribution system (WDS), of which the numerical method is relatively ripe [16–18]. One is that in the WDS, the water is often assumed to be incompressible, while in the PTSF, the expansion and contraction of the HTF are non-negligible due to the significant temperature difference. The other is that the flow resistance is considered as a constant or merely a function of the flow velocity in the WDS, while it is a more complex function under the influence of temperature variation in the PTSF.

Besides, developing an effective control strategy of the PTSF is also dependent on the integrality of the thermal hydraulic model. Ref. [19] pointed out that the header control valves (HCVs) are used to control the flow rate and outlet temperature of the subfield in a real operated PTSTPP. [13] indicated that the automatic balancing valves can be used for PTSF control when the spatial variation of solar irradiance is an issue. Refs. [14] and [20] indicated that the loop control valves (LCVs) have the potential to improve the PTSF performance. However, the lack of a refined model increases the difficulty of calculating the valves opening and simulating the PTSF characteristics under varied solar irradiance.

To overcome the above problems, as well as improve the operational performance and controllability of the PTSTPP, a comprehensive thermal hydraulic model (CTHM) of the PTSF based on a pilot plant in Beijing is presented in this paper. The CTHM is improved based on the THDM developed in [15]. The optical and thermal analysis of the PTC, the flow characteristics of pipe, pipe fitting, pump, and the valves are all considered in the CTHM. A novel numerical method, which is based on graph theory and the Newton–Raphson method, is developed to solve the CTHM. Moreover, a cold test and a hot test are implemented to validate the CTHM under thermal and hydraulic disturbance.

Compared with the THDM and other existing models, the CTHM has three main advantages. Firstly, adding the pump module establishes the relationship among the pump capacity, flow resistance, and the temperature. This improvement further makes the required input parameters get rid of the dependence on the total flow rate. Secondly, the CTHM contains both the hydraulic and thermal inertia, and this leads to more accurate results in the transient simulation. Finally, a more comprehensive model can widen and deepen the research on the PTSF; the CTHM can be applied to simulate the behavior of the PTSF under various disturbances and study the control strategy of the PTSF under uniform or nonuniform solar irradiance.

2. Description of the PTSF of a 1 MW Pilot Plant

The Badaling parabolic trough solar power pilot plant, which is the first operational PTC solar thermal plant on the MW scale in China, is situated in Yanqing at a latitude of 40.5 °N and a longitude of 115.94 °E. A view of the pilot plant is shown in Figure 1.



Figure 1. View of the Badaling parabolic trough solar power pilot plant.

As illustrated in Figure 2, two east–west layout loops (Loop 1 and Loop 3) with 4150 m long solar collector assemblies (SCAs) and one south–north layout loop (Loop 2) with 6100 m long SCAs together form the principal part of the PTSF. Besides, an extra pipe is placed in Loop 2 for a study of flow balance [15]. An HCV and three LCVs are used to manipulate the total flow rate and flow distribution. A kind of synthetic oil named Therminol VP-1, of which the physical properties can be fitted into some polynomials in temperature based on the tested data [13], is used as the HTF in the pilot plant, while the more detailed information about the physical properties of the HTF is summarized in Appendix A.

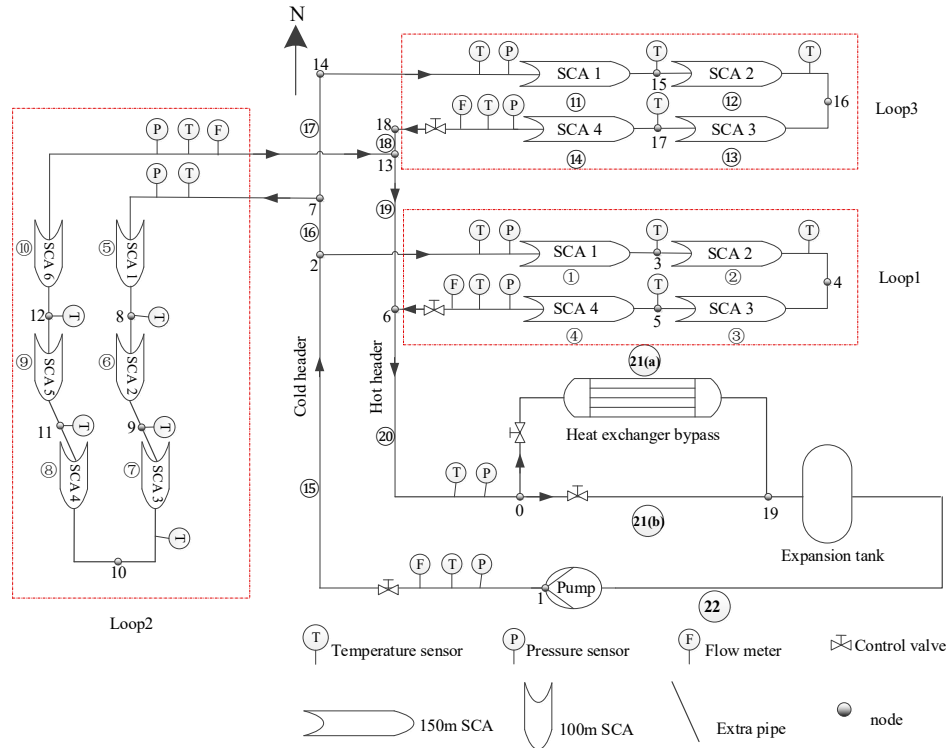


Figure 2. Flow diagram, nodes, and pipe section label of the parabolic trough solar field (PTSF) in the pilot plant.

The present study involves two kinds of pipes in the PTSF, i.e., the absorbed pipe covered with an evacuated glass envelope, and the insulated pipe (header). Hereafter, the symbols, which are concerned with the pipe, will represent the former with the subscript *abs*, and represent the latter with the subscript *ins*. Moreover, the symbols without any subscripts mean that they are universal for both types. Specific characteristics of the PTC, header, pump, and valve are described in more detail below.

2.1. The PTC and Header

In the relevant published studies [1–12], the thermal model of the PTC developed in [7] is applied in this paper. The effectiveness of this model has been validated by the tested data regardless of the simplified thermal loss of the PTC [7,15].

As shown in Figure 3a, the energy equation of the control volume with an axial length of Δx can be given by [7]:

$$\rho_{abs} A_{abs} c_{abs} \frac{\partial \bar{T}_{abs}}{\partial t} = P_{use} - H_{l,abs}(\bar{T}_{abs}) - D_{abs} \pi h(\bar{T}_{abs} - \bar{T}_f) \quad (1)$$

$$\Delta x A_f \bar{\rho}_f \bar{c}_f \frac{\partial \bar{T}_f}{\partial t} + c_{f,out} \rho_{out} Q_{f,out} T_{f,out} - c_{f,in} \rho_{in} Q_{f,in} T_{f,in} = \Delta x D_{abs} \pi h(\bar{T}_{abs} - \bar{T}_f) \quad (2)$$

where the subscript *f* represents the HTF, Q , ρ , T , and c represent the volume flow rate, density, temperature, and specific heat capacity, and D and A are the diameter and sectional area. $H_{l,abs}$ represents the heat loss of the absorber per meter, which is caused by the temperature difference between the absorber tube and the exterior glass envelope, and can be simplified as a polynomial in T_{abs} .

P_{use} in Equation (1) is the solar thermal power supplied to the absorbed pipe per meter, which is given by [21]:

$$P_{use} = W_{col} I \kappa(\theta) \eta_o f_{shd} f_{end} \tag{3}$$

$$\eta_o = \beta r_{cl} \tau \alpha \gamma$$

where W_{col} represents the collector width, I represents the direct normal irradiance (DNI), and κ is the incidence angle (θ) modifier, which is used to account for all geometric and optical losses because of an incident angle of more than 0° . η_o is the optical efficiency of the PTC, which is the product of the clean mirror reflectivity (r_{cl}), the transmittance of the glass envelope (τ), the absorbance of the absorber pipe (α), and the intercept factor (γ). β is the defocused factor, which is used for considering the loss of efficiency caused by the difference between the actual and desired tracking angle. As shown in Figure 3c, the trend of β can be simulated by the Solartrace tool [3]. f_{end} and f_{shd} are two factors due to end loss and row shadowing; the schematic diagram of f_{end} and f_{shd} is shown in Figure 3a,b respectively. Expressions of these two factors can be given by [3]:

$$f_{end} = 1 - \frac{l_{fl} \tan(\theta)}{l_{SCA}} \tag{4}$$

$$f_{shd} = \min \left[\max \left(0; \frac{l_{rs} \cos(\omega)}{W_{col} \cos(\theta)} \right); 1 \right] \tag{5}$$

where ω represents the zenith angle, and l_{SCA} , l_{rs} , and l_{fd} are the length of the SCA, row spacing, and focal distance, respectively.

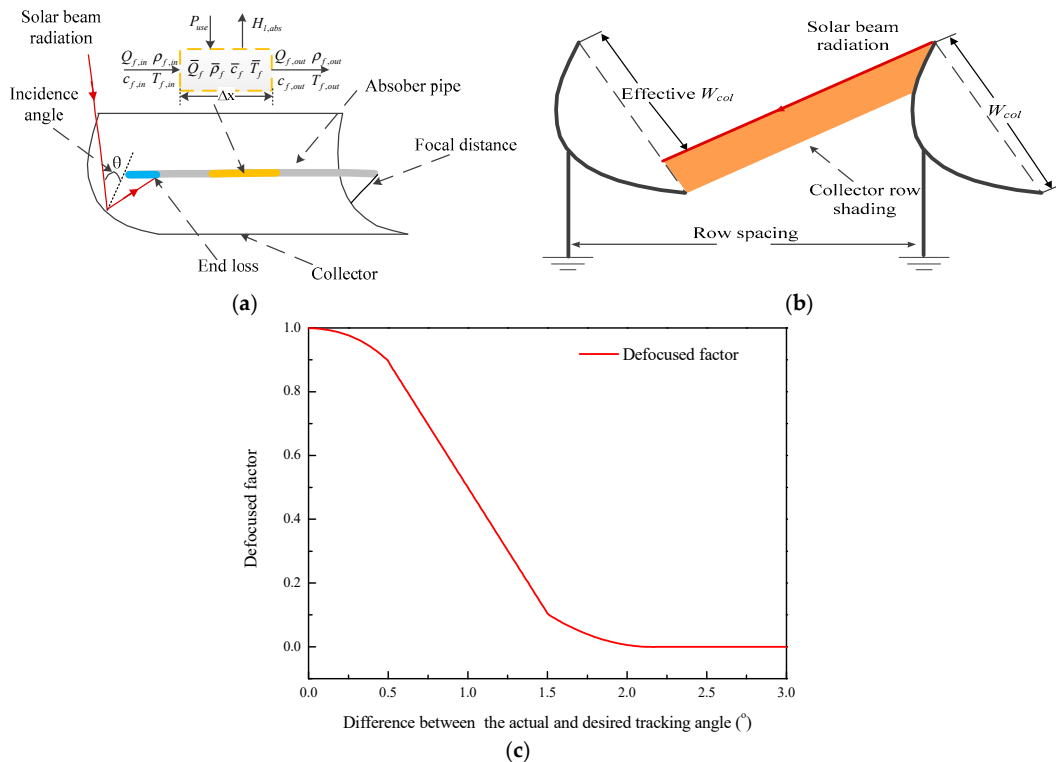


Figure 3. Thermal and optical analysis of the parabolic trough collectors (PTC) for (a) control volume and end loss; (b) row shading; and (c) trend of the defocused factor.

h in equations (1) and (2) is the convection heat transfer coefficient between the absorber inner surface and the HTF, which can be given by [4]:

$$h_{conv} = Nu_f \frac{k_f}{D_{abs}} \tag{6}$$

$$Nu_{abs} = \frac{f_{abs} / 8(Re_{abs} - 1000)Pr_f}{1 + 12.7\sqrt{f_{abs} / 8(Pr_f^{2/3} - 1)}} \left(\frac{Pr_f}{Pr_{abs}} \right) \quad (7)$$

$$f_{abs} = (1.82 \log_{10}(Re_{abs}) - 1.64)^2 \quad (8)$$

where Re , Nu , and Pr are the Reynolds number, Nusselt number, and Prandtl number, respectively. k is the thermal conductivity. In the normal operation of the pilot plant, the variation range of the Re and Pr are about $1 \times 10^4 < Re < 9 \times 10^5$ and $4.5 < Pr < 45$; these two parameters are within the range of application of Equation (8), which is valid for $2300 < Re < 5 \times 10^6$ and $0.5 < Pr < 2000$ [4].

More than the HCE absorber pipes, thermal losses exist in the insulated pipes (headers). In this work, the mineral wool is used as the thermal insulation material, and the thermal losses of the insulated pipes can be calculated under an assumption of neglecting the thermal resistances of the exterior air film and pipe walls [21], which is given by:

$$\begin{aligned} & A_{ins} l \bar{\rho}_f \bar{c}_f \frac{\partial \bar{T}_f}{\partial t} + c_{f,out} \rho_{f,out} Q_{f,out} T_{f,out} - c_{f,in} \rho_{f,in} Q_{f,in} T_{f,in} \\ & = 2\pi l \frac{\bar{k}_{ins}}{\ln((D_{ins} + 2\delta) / D_{ins})} (T_a - \bar{T}_f) \end{aligned} \quad (9)$$

where \bar{k}_{ins} is the thermal conductivity of the pipe insulation at the average temperature of \bar{T}_f and T_{ins} , and T_a and δ are the insulation thickness and ambient temperature, respectively. The value of \bar{k}_{ins} can be fitted into a polynomial at the average temperature [21].

The thermal and optical parameters, the geometry of the absorber and the header are listed in Table 1, where formulas of the incidence angle modifier is given by [21], and formulas of the heat loss r is supplied by the manufacturer. Other header parameters that are not included in the table, such as the length from pump to Loop 1, the length from Loop 3 to expansion, the expression of \bar{k}_{ins} , and so on, can be measured from the design drawing.

Table 1. Main parameters of the collector, absorber, and header.

Pipe	Item	Value/Expression
Collector	Length (m)	100/150
	Width (m)	5.776
	Focal length (m)	1.71
	Clean mirror reflectivity	0.96
	Ideal intercept factor	0.8268
	Incidence angle modifier	$\cos(\theta) - 5.25027 \times 10^{-4} \theta - 2.859621 \times 10^{-5} \theta^2$ [21]
	Row spacing (m)	20
Absorber	Inner diameter of the absorber tube (m)	0.064
	Outer diameter of the absorber tube (m)	0.07
	Absorber absorptivity	0.95
	Transmittance of the glass envelope	0.95
	Heat loss (W/m)	$5.2569 \times 10^{-6} T_{abs}^3 - 0.0012 T_{abs}^2 + 0.1343 T_{abs} + 13.7484$ [15]
Header	Inner diameter of the header (m)	0.125
	Total extra pipe length (m)	190
	Inner diameter of the extra pipe (m)	0.069

Insulation thickness (m)	0.15
Thermal conductivity of the mineral wool ($W m^{-1} K^{-1}$)	$6.02 \times 10^{-7} \bar{T}_f^3 - 2.146 \times 10^{-5} \bar{T}_f^2 + 0.194 \bar{T}_f + 26.5$ [21]

Equations (1)–(9) together form the thermal part of the CTHM, this part is applied to simulate the outlet temperature and update the properties of the HTF.

2.2. Pump and Valve

As shown in Figure 4a, a canned centrifugal pump is chosen to circulate the HTF in the pilot plant, the capacity, head, and efficiency at design condition are 99 m³/h, 200 m, and 45%, respectively. In normal hydraulic calculations, the pump head is usually fitted into a polynomial in the capacity according to the pump’s performance curve, and this method has been applied to the PTSF by defining the polynomial with a series of universal coefficients [22,23]. In this study, as shown in Figure 4b, the polynomial of the pump head can be given in a more specific way based on the pump’s performance curve supplied by the manufacturer.

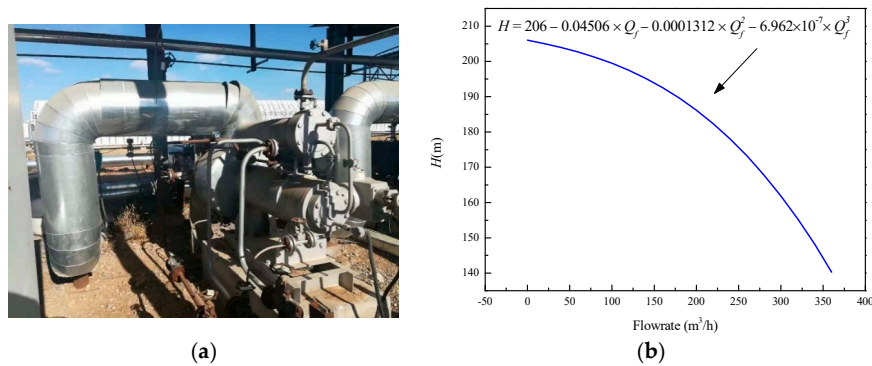


Figure 4. (a) View of pump; (b) pump’s performance curve.

A typical control valve in the PTSF is shown in Figure 5a, the electric actuator manipulates the opening of the valve. In general, as shown in Figure 5b, the control valve has three inherent flow characteristics [24], i.e., linear, quick open, and equal percentage. In the pilot plant, both the LCVs and HCVs are chosen to have the flow characteristics with equal percentage.

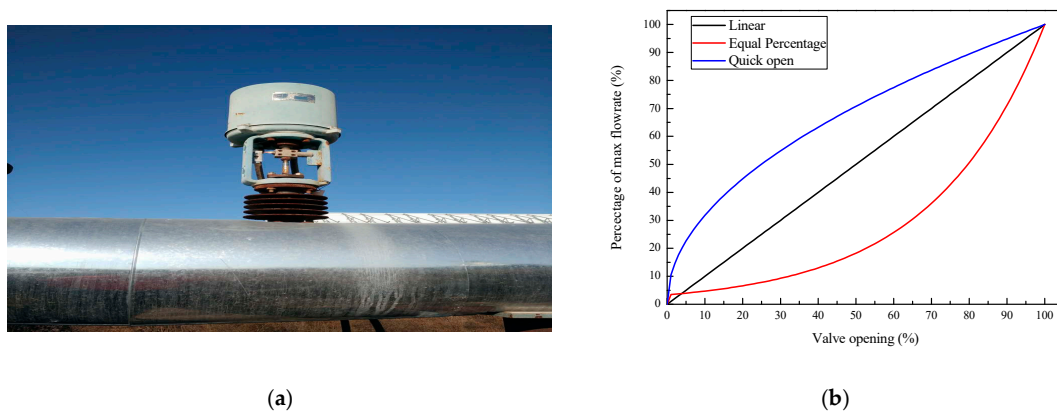


Figure 5. (a) View of the control valve; (b) three inherent flow characteristics of the control valve.

2.3. Measurement and Uncertainty

In the PTSF of the pilot plant, the DNI, flow rate, temperature, and pressure of the HTF in the header and three loops, the opening of the valve, the actual tracking angle, and the ambient temperature are the main parameters that need to be measured; the information of measurements and their uncertainty are summarized in Table 2.

Table 2. Information about the measurements. DNI: direct normal irradiance.

Parameters	DNI	Temperature	Pressure	Flow Rate	Valve Opening	Tracking Angle
Measurements	Pyrheliometer model CH1 by Kipp and Zonen	Pt 100 class B	Pressure transmitters	Yewflo flowmeter	Electrical signals	Inclinometer
Uncertainty/Accuracy	0.5%	<2.3 °C	0.2%	1%	5%	<0.001 °C

3. Hydraulic Model Description

3.1. Hydraulic Model in the Single Pipe

The schematic of the control volume of the hydraulic model is shown in Figure 6, in which p and ν represent the pressure and kinematic viscosity of the HTF, respectively. The continuity equation of the control volume with a length of Δx can be given by [25]:

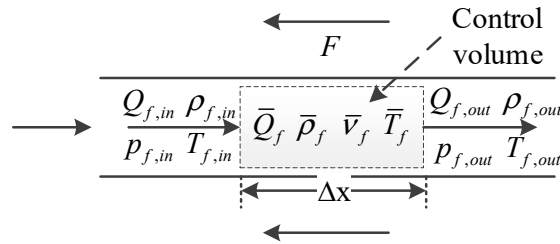


Figure 6. Control volume of the hydraulic model.

$$A\Delta x \frac{\partial \bar{\rho}_f}{\partial t} = \rho_{f,in} Q_{f,in} - \rho_{f,out} Q_{f,out} \quad (10)$$

where the left-hand side is caused by the thermal transients.

The momentum equation of the control volume in Figure 6 can be given by [25]:

$$\begin{aligned} \left(\frac{\Delta x}{A}\right) \bar{Q}_f \frac{\partial \bar{\rho}_f}{\partial t} + \left(\frac{\Delta x}{A}\right) \bar{\rho}_f \frac{\partial \bar{Q}_f}{\partial t} + \frac{\rho_{f,out} Q_{f,out}^2}{A^2} - \frac{\rho_{f,in} Q_{f,in}^2}{A^2} \\ = p_{f,in} - p_{f,out} - F + \bar{\rho}_f gH \end{aligned} \quad (11)$$

The first two terms on the left-hand side of Equation (11) are caused by the thermal transients and hydraulic transients, respectively. F , which represents the flow loss, can be given by:

$$\begin{aligned} F &= S \bar{Q}_f^2 \\ S &= S_p + \sum_{i=1}^{N_{fit}} S_{fit,i} + S_{va} \end{aligned} \quad (12)$$

where S represents the total flow resistance in the control volume, which can be caused by the pipe wall (S_p), pipe fitting (S_{fit}), and valve (S_{va}). S_p can be calculated using the Darcy–Weisbach equation [26]:

$$\begin{aligned}
 S_p &= \frac{1}{2} \bar{\rho}_f f \left(\frac{l}{DA^2} \right) \frac{1}{2} \\
 f &= 8 \left(\left(\frac{8}{Re} \right)^{12} + \frac{1}{B^{1.5}} \right)^{\frac{1}{12}} \\
 B &= \left(2.457 \ln \left(\frac{1}{(7/Re)^{0.9} + 0.27(\epsilon/D)} \right) \right)^{16} + \left(\frac{37530}{Re} \right)^{16}
 \end{aligned} \tag{13}$$

where f is the inner friction factor of the pipe, which is an empirical formula for the Reynolds number (Re) and absolute roughness of the pipe (ϵ) [27].

Analogously, S_{fit} can be given by [26]:

$$S_{fit} = \frac{1}{2} K_{fit} \frac{\bar{\rho}_f}{A^2} \tag{14}$$

where K_{fit} is the pressure drop coefficient of the fitting. The elbow and ball joint are the two main fittings in the PTSF; their K_{fit} values are 0.75 and 0.6 according to the manufacturer.

S_{va} is a function of the opening of the control valve (op), for the LCVs and HCVs, of which the equal percentage of flow characteristics, S_{va} , can be calculated by [24]:

$$S_{va} = 100 \bar{\rho}_f \left(\frac{3600}{R^{(op-1)} G_{max}} \right)^2 \tag{15}$$

where G_{max} represents the max flow coefficient of the valve, and R represents the rangeability. The G_{max} values of LCVs and HCVs are 68 m³/h and 158 m³/h, respectively. The R of both the LCVs and HCVs are 30.

3.2. Matrix Representation of Pipe Network

Graph theory has been one of the most powerful tools for pipe network analysis due to its convenience and effectiveness [18]; therefore, this method is used to calculate the hydraulic part of the PTSF in the present study.

Before building the specific equation, a key concept in the graph theory, which is called the incidence matrix, must be introduced first. If a pipe network contains n nodes and b pipe sections, accordingly, the incidence matrix M is an $n \times b$ order matrix that can be expressed as [18]:

$$\mathbf{M}^{(ij)} = \begin{cases} +1 & \text{if pipe } j \text{ starts at node } i \\ 0 & \text{if pipe } j \text{ is not connected to node } i \\ -1 & \text{if pipe } j \text{ ends at node } i \end{cases} \tag{16}$$

In the PTSF, the nodes can be divided into two types; one is that of which the pressure is a reference pressure (type 0 with the subscript 0), the other is that the node pressure is unknown (type 1 with the subscript 1). Hence, there are four types of incidence matrix in the PTSF: $M_{0,in}$, $M_{0,out}$, $M_{1,in}$, and $M_{1,out}$. Moreover, all of the equations will be discretized with the implicit difference method in time. For the pilot plant, the detailed information about point and pipe labels is shown in Figure 2; choosing pipe 21 (a) or 21 (b) depends on the outlet temperature and thermal requirement.

According to the graph theory, the continuity equation of a type 1 node can be expressed by:

$$M_{1,in} \mathbf{Q}_{f,in}^t + M_{1,out} \mathbf{Q}_{f,out}^t = \mathbf{q}_1^t \tag{17}$$

where $\mathbf{Q}_{f,in}$ and $\mathbf{Q}_{f,out}$ are the inlet and outlet flowrate vectors, respectively. \mathbf{q}_1 is the type 1 nodal out flow rate vector.

According to Equation (10), the continuity equation of the pipe section can be expressed as:

$$D(\rho_{f,out}^t) Q_{f,out}^t - D(\rho_{f,in}^t) Q_{f,in}^t = D(V) \frac{(\bar{\rho}_f - \bar{\rho}_f^t)}{\Delta t} \quad (18)$$

where $D()$ in this paper means diagonalizing the vector in the bracket. $\rho_{f,in}^t$, $\rho_{f,out}^t$, and $\bar{\rho}_f$ are the inlet, outlet, and average density vector of the HTF, respectively. V is the volume vector, of which the i th element is:

$$V^{(i)} = l^{(i)} A^{(i)} \quad (19)$$

where l and A are the length vector and sectional area vector of the pipe.

Analogously, based on Equation (11), the momentum equation of the pipe network can be expressed as:

$$\begin{aligned} & D(A_c) \bar{Q}_f^t - D(B_c) \bar{Q}_f^t + \frac{D(\rho_{f,out}^t) D(|Q_{f,out}^t|) Q_{f,out}^t}{D^2(A)} - \frac{D(\rho_{f,in}^t) D(|Q_{f,in}^t|) Q_{f,in}^t}{D^2(A)} \\ &= (M_{1,in} + M_{1,out})^T p_1^t + (M_{0,in} + M_{0,out})^T p_0^t - D(S) D(|\bar{Q}_f^t|) \bar{Q}_f^t + gD(\bar{\rho}_f) H \\ & A_c^{(i)} = \frac{l^{(i)} 2\bar{\rho}_f^{t,(i)} - \bar{\rho}_f^{(i)}}{A^{(i)} \Delta t} \\ & B_c^{(i)} = \frac{l^{(i)} \bar{\rho}_f^{t,(i)}}{A^{(i)} \Delta t} \end{aligned} \quad (20)$$

where \bar{Q}_f^t is the average flow rate vector, p_1 and p_0 are the pressure vector of node type 1 and type 0, S is the flow resistance vector, and H is the pump head vector.

3.3. Numerical Method

Equations (10)–(20) form the hydraulic part of the CTHM, which can be used to simulate the flow distribution, pressure drop, and pump head of the PTSF. The hydraulic part together with the thermal part mentioned in Section 2 constitute an entire CTHM. Two difficulties must be solved first before simulating with the CTHM. One is how to decouple the thermal part and the hydraulic part, and the other is how to solve the complex matrix equations in the hydraulic part conveniently and quickly. An iterative approach referred to in [15] is applied to solve the first question. Firstly, we calculate the temperature used the thermal model at an initial flow rate distribution; then, we plug the updated temperature to the hydraulic part to update the physical properties of the HTF and calculate the hydraulic parameters. This process will continue until the calculated flow distribution converges to a given tolerance. For the second difficulty, a method based on matrix theory and the Newton–Raphson method is applied to solve the hydraulic matrix equations; this method is derived from [18] and improved in this work through adding the expansion and extraction of the HTF and the varying flow resistance due to the temperature change. The detailed procedure of this method is presented in Appendix B as an innovation of this study.

According to the above content, a detailed flow chart of the CTHM is shown in Figure 7. Besides containing both the hydraulic and thermal transients, another advantage of the CTHM is that the simulation no longer depends on the inlet flow rate of the header due to the newly added pump module.

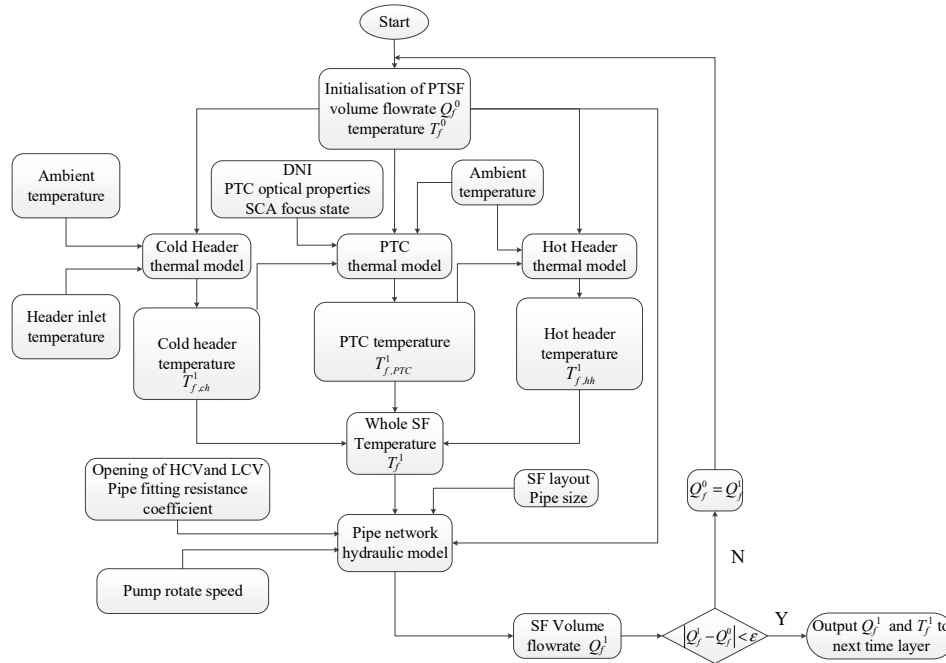


Figure 7. Flow chart of the comprehensive thermal hydraulic model (CTHM).

4. Validation Results and Discussion

In present work, a cold test and a hot test based on the pilot plant were conducted to validate the CTHM. The cold test was used to validate the hydraulic characteristics of the CTHM; the transient hydraulic effects are caused by periodically varying the opening of the LCVs. Both the hydraulic and thermal characteristics of the CTHM are validated through the hot test; hence, in addition to the periodically varying opening of the LCVs, the loop collectors are operating at concentrating status to cause the thermal transient effects. More detailed information about these two tests is summarized in Table 3. The simulation is implemented in MATLAB®. For the CTHM, Figure 7 shows the main input parameters: the header inlet temperature, DNI, ambient temperature, and the actual tracking angle of the SCA; the main output parameters that need to be validated are the total flow rate, flow rate distribution in each loop, pressure drop, and the outlet temperature of each loop. The uncertainty or accuracy of the measurements of all these parameters can be found in Table 2 for future discussion.

Table 3. The detailed summarized information of the two tests.

	Cold Test	Hot Test
Validation target	Transient hydraulic characteristics	Both the transient hydraulic and thermal characteristics
Collectors status	All loops defocused totally	Loop 1 and Loop 3 concentrated totally Loop 2 defocused totally
Loop control valves status	Loop 1 and Loop 3 varying the opening of the LCV periodically Loop 2 keeping the opening of the LCV fully open	
Pump operating condition		Full load
Parameters to be validated	The inlet flow rate of header and all three loops Pressure drop between cold and hot header	The inlet flow rate of header and all three loops The outlet temperature of all three loops Pressure drop between cold and hot header

4.1. Cold Test

The cold test was conducted from 9:41:39 to 11:30:00 on 22 August 2018; as mentioned in Table 3 and shown in Figure 8, the opening of LCVs in Loop 1 and Loop 3 varied between 50–100% with a change rate of about 5% every 12 s, which is considered a moderate frequency (a too high frequency may cause a water hammer event, and a too-low frequency will obscure the transient hydraulic effect). Due to the lack of a valve automatic control device, the manual operations reduced a bit of the accuracy and simultaneity of the periodic variation.

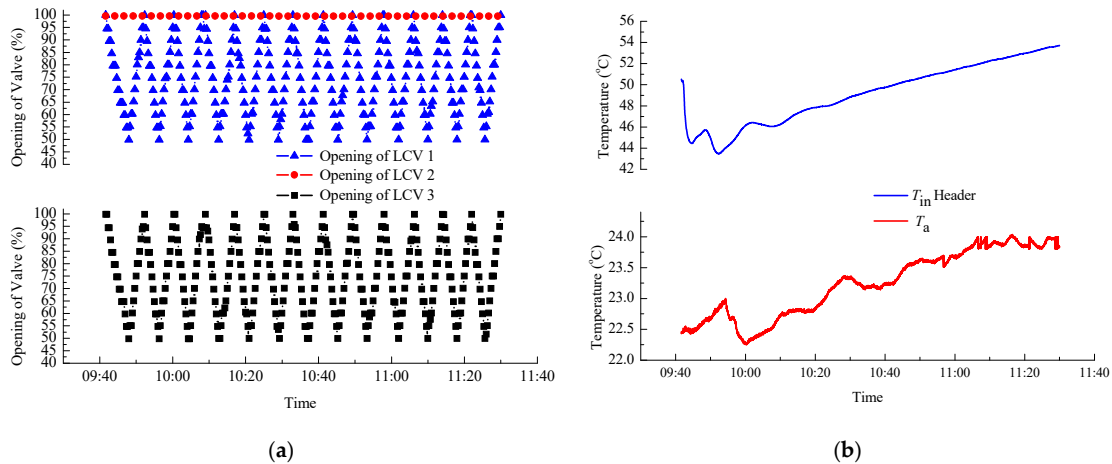


Figure 8. Measured initial data in the cold test: (a) opening of three LCVs; (b) ambient and header inlet temperature.

Figure 9a shows that the calculated header inlet flow rate is slightly greater than the measured rate with a small root mean square error (RMSE). The error is likely caused by an underestimation of the pressure drop, because some local pressure loss such as the contraction or expansion of the pipe is not considered in the model. This view can be verified by Figure 9b, where the calculated pressure drop of the header is lower than the measured value. Figure 9 also presents the inlet flow rate, and the pressure drop varies at the same frequency, which is similar to the opening of the LCVs. This is because the periodical change of the valve opening varies the total flow resistance of the PTSF and further impacts the pump head and capacity.

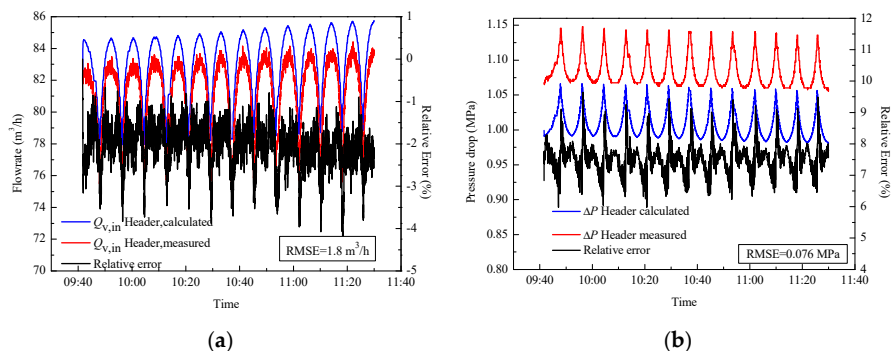


Figure 9. Compared results between calculated and measured data in a cold test for the (a) header inlet flow rate, and (b) header pressure drop.

Besides the total flow rate in the header, simulating the flow distribution in loops is another essential function for the CTHM that needs to be calculated and validated. Good agreement between the calculated results and measured data is shown in Figure 10a–c; the RMSEs for the outlet flowrate

of loops 1 to 3 are $1.75 \text{ m}^3/\text{h}$, $0.86 \text{ m}^3/\text{h}$, and $0.97 \text{ m}^3/\text{h}$, respectively. The uncertainty of the electric control valve actuators with a value of 5% (shown in Table 2) is considered as the primary error sources. Besides, Figure 10 shows that the discrepancy is changing with the flow rate; this is due to Equation (16), which can cause different errors in the different flow rates and Re values [27]. The relative errors shown in Figure 10d can make this clear: when the valve opening varied, the relative errors present almost simultaneous fluctuations. Another noticeable feature presented in Figure 10b is that the outlet flow rate of Loop 2 has a lower value and opposite trend compared to the other two loops. The lower value is caused by an extra loop in Loop 2 that can increase the flow resistance of Loop 2 and diminish the flow rate. The opposite trend occurs because when the valve openings in Loop 1 and Loop 3 decreased, the relative value of the flow resistance of Loop 2 changed from the larger one to the smaller one; although the header inlet flow rate decreased during this process, Loop 2 could be distributed a greater flow rate due to its smaller flow resistance.

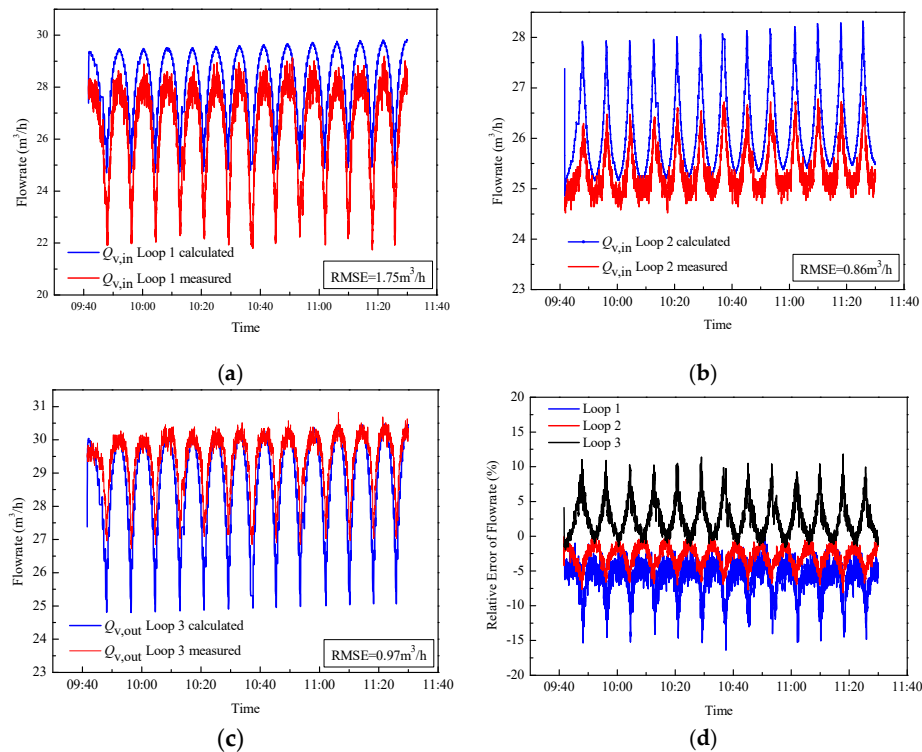


Figure 10. Compared results between calculated and measured data in cold test for (a–c): the outlet flow rate of loops 1 to 3; and (d) the relative errors of flow rate.

4.2. Hot Test

The hot test was conducted from 09:50 to 11:30 on 23 August 2018. As shown in Figure 11a, the opening of LCVs varies similarly to the cold test in addition to an intermission at about 10:50; this is because the operator should open the heat exchange bypass in case of overheating the HTF at this moment, and this operation also leads to the decreasing of the inlet temperature of the header, as shown in Figure 11b.

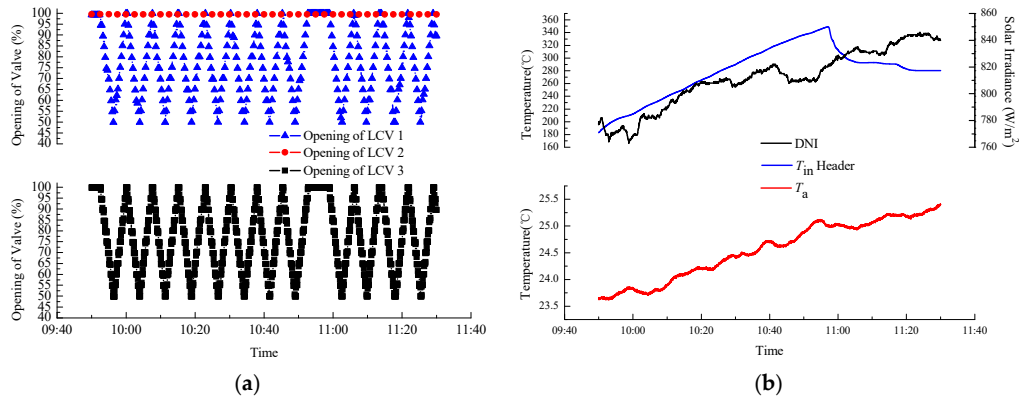


Figure 11. Measured data in the hot test: (a) opening of three LCVs and DNI; (b) ambient and header inlet temperature.

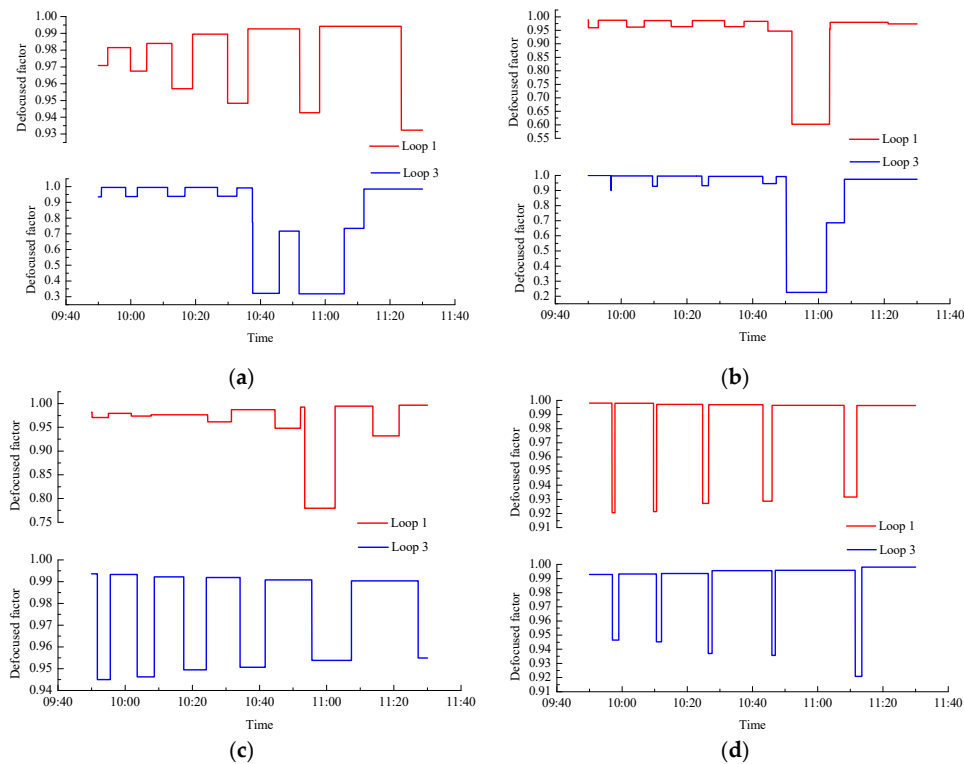


Figure 12. Defocused factor of the solar collector assemblies (SCAs) in Loop 1 and Loop 3: (a–d) SCA 1 to 4.

Compared with the cold test, the parameters referring to the solar irradiance absorption must be measured firstly in the hot test. The measured DNI is shown in Figure 11b, and the defocused factor of the SCAs in Loop 1 and Loop 3, which are measured by the inclinometer and calculated according to Figure 3c, are presented in Figure 12.

As shown in Figure 13, errors regarding the compared inlet flow rate and pressure drop present obvious differences before and after the opening of the exchange bypass; this is due to the misestimate of the flow resistance in the exchange bypass pipe. Compared with the cold test (Figure 9), the hot test has a greater inlet flow rate and lower pressure drop, which is mainly because the HTF has a lower viscosity at a higher temperature.

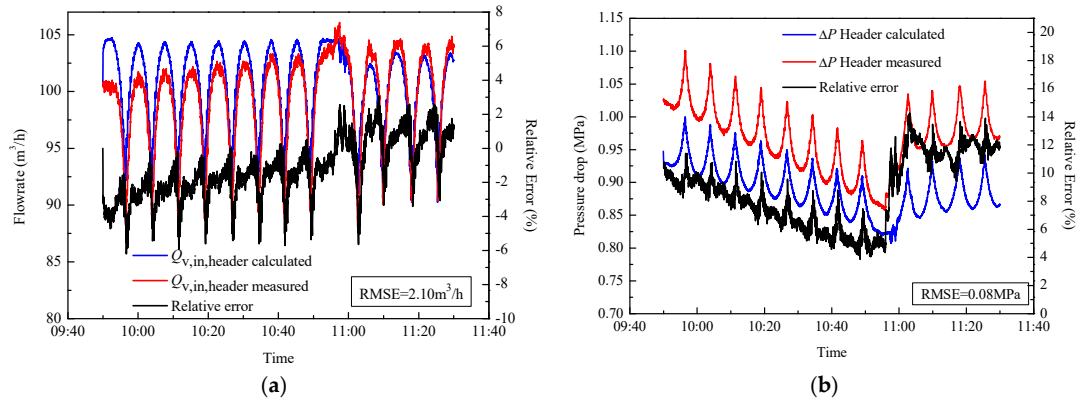


Figure 13. Compared results between calculated and measured data in a hot test for the (a) header inlet flow rate, and (b) header pressure drop.

As shown in Figure 14, the calculated flow rate distribution maintains good consistency with the measured data in the hot test, the RMSEs for the outlet flow rate of loops 1 to 3 are 1.82 m³/h, 1.01 m³/h, and 1.50 m³/h, respectively. Compared with the cold test, there are two extra sources that cause the error. The one is that the larger outlet flow rate of the header will magnify the error caused by the uncertainty of electric control valve actuators; another is that the error of the calculated temperature will influence the flow resistance distribution of the PTSE, and then increase the error of the flow rate.

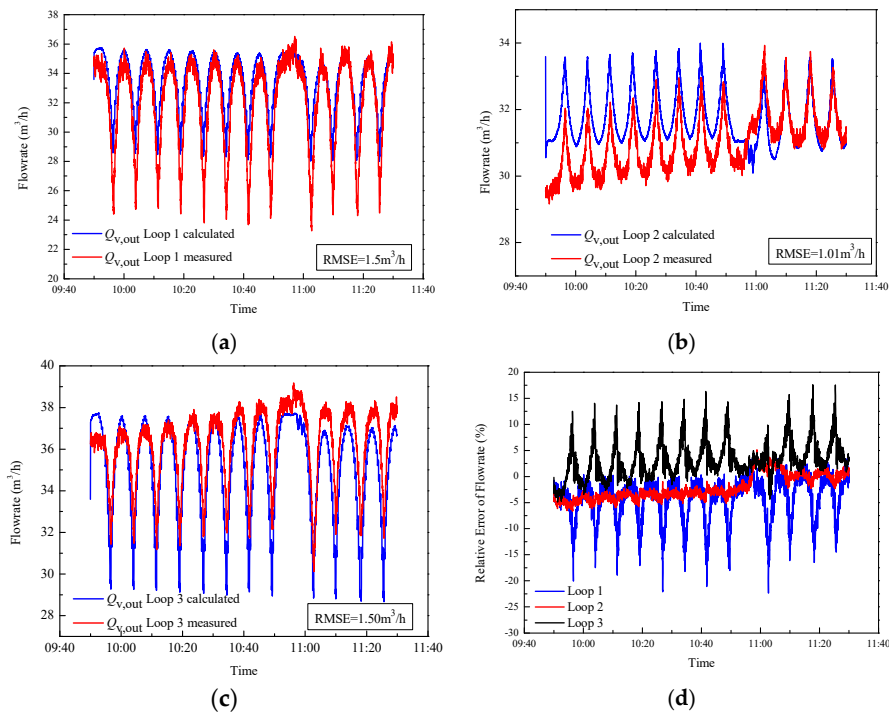


Figure 14. Compared results between calculated and measured data in a hot test for (a–c): the outlet flow rate of loops 1 to 3; and (d) the relative errors of the flow rate.

Figure 15 shows that the RMSEs for the calculated outlet temperatures of three loops were 8.54 °C, 6.30 °C, and 8.14 °C, respectively. This good agreement mainly benefited from the precisely calculated flow rate distribution and the accuracy of the thermal part in the CTHM. Despite the fluctuated flow rate, the great thermal inertia of the PTSE made the temperature trend present a relatively smooth curve. Besides the initialization temperature, which caused the discrepancies within the first 10 min, there are two reasons for the error in calculating the outlet temperature. One

is that the flow rate error will accumulate along with the results of the outlet temperature. Another one is that the installation error of the SCAs will cause the discrepancies of outlet temperature within some short periods of time [28], such as Loop 1 from 10:50 to 11:10 and Loop 3 from 10:40 to 11:00.

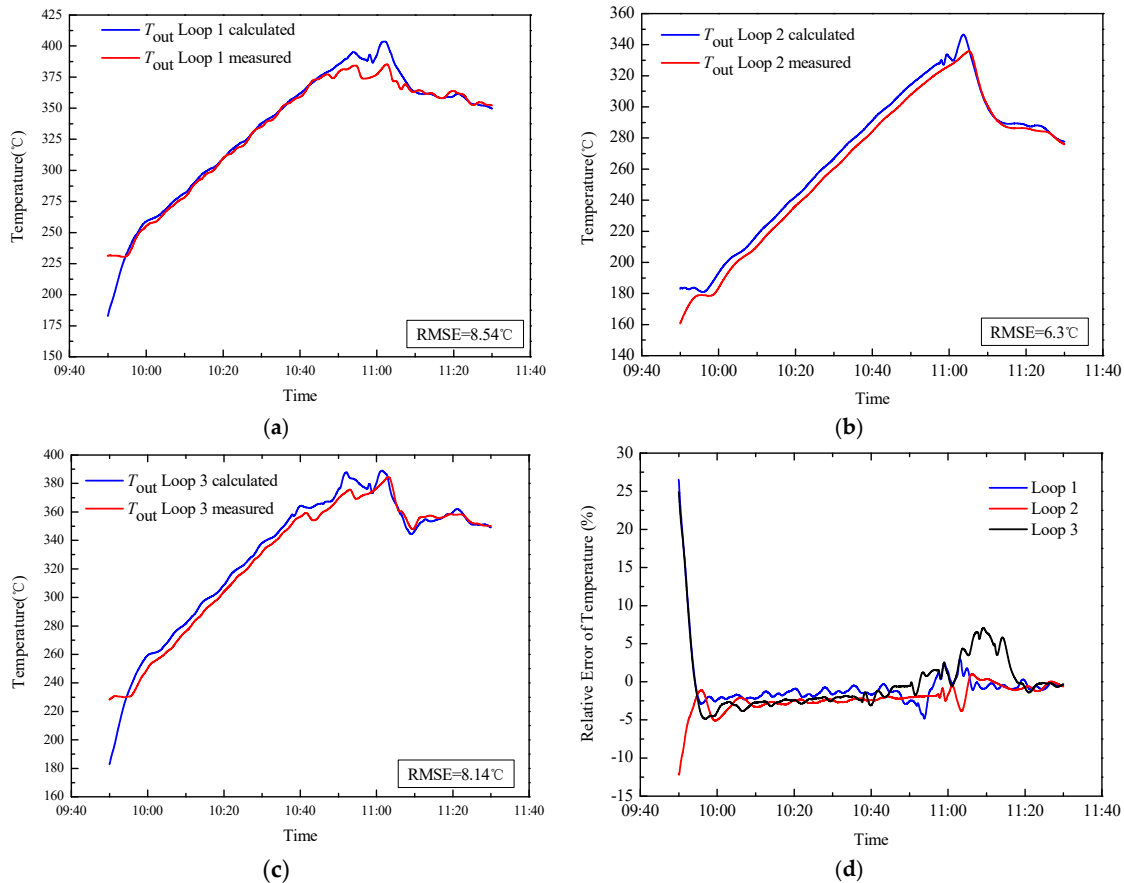


Figure 15. Compared results between calculated and measured data in hot test for (a–c): the outlet temperature of loops 1 to 3; and (d) the relative temperature errors.

5. Model Applications

After the accuracy and availability of the CTHM are validated, two potential abilities of the model are presented in this section. First, the relationship between the thermal and hydraulic transients are revealed by two simulating cases. Secondly, two simple feedforward control strategies are introduced and verified through the CTHM. In all of the simulations, the ambient temperature and inlet temperature of the header remain 25 °C and 290 °C, respectively.

5.1. Transients Simulating

As a complex piping network, the thermal effect is the biggest difference between the WDS and the PTSF. Two cases are conducted to simulate how the thermal transients influence the hydraulic state. Ma et.al [15] pointed out that the PTSF of the pilot plant can achieve balanced flow distribution when the openings of the three LCVs are 58%, 100%, and 60%, respectively; these values will be maintained in these two cases.

Case 1, which lasts for 1.3 h, is implemented for simulating the impacts of DNI saltation on the total flow rate and pump pressurizing of the PTSF. As shown in Figure 16a, the DNI changes from 0 to 800 W/m² at 0.4 h and turns back into 0 at 0.9 h, and these two disturbances cause a drastic fluctuation in the header flow rate, as shown in Figure 16b. At 0.4 h, as shown in Figure 16b, the inlet and outlet header flow rate present two different trends. The peaking of heat gain causes an

expansion of the HTF and further leads to the increasing velocity; this will result in an increase of the pump pressurizing (as shown in Figure 16c) and a reduction of pump capacity (inlet header flow rate). Meanwhile, the viscosity of the HTF decreases with the temperature rise (as shown in Figure 16d). Together with the density and viscosity, the total flow resistance and pump pressurizing will reach a local maximum and begin to decrease; when the effect of expansion surpasses the effect of viscosity reduction, the total pressure drop increases again, and the pump capacity decreases until it reaches a steady state. Similar reasons can demonstrate the fluctuation of the header inlet flow rate, and pump pressurizing happens when the DNI vanishes. For the header outlet flow rate, according to Equation (12), the dramatic expansion and contraction of the HTF caused by the DNI saltation will be embodied in the outlet flow rate, which causes an opposite trend between the inlet and outlet flow rate.

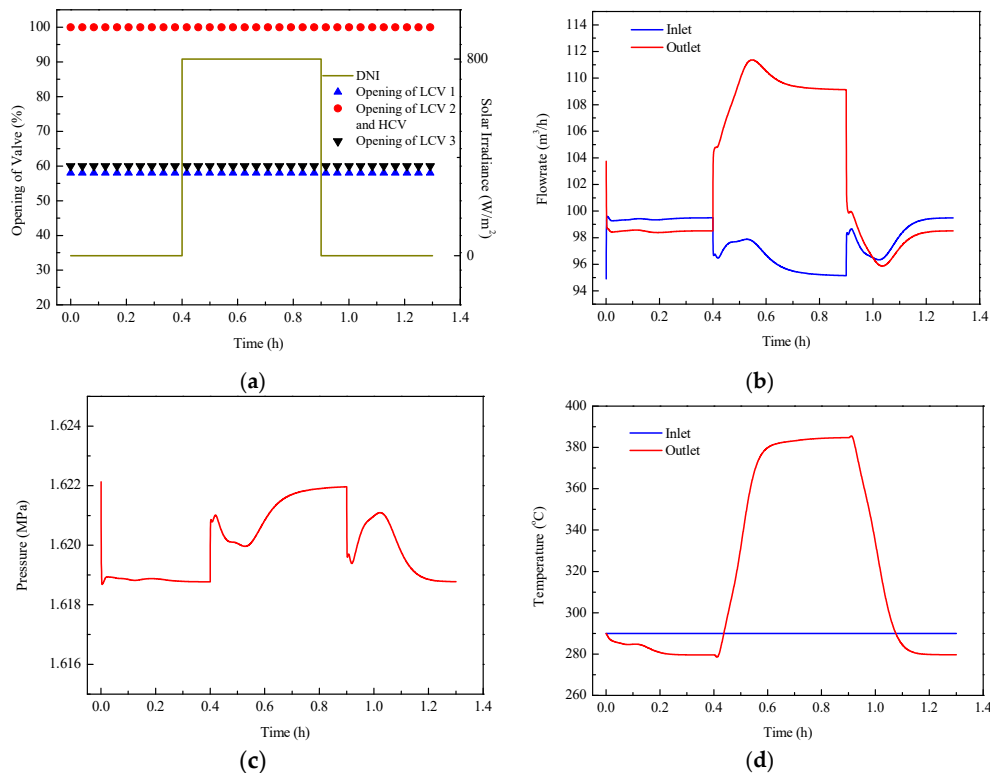


Figure 16. Simulating Case 1 for (a) initial parameters, (b) inlet and outlet header flow rate results; (c) pump pressurizing results, and (d) inlet and outlet header temperature results.

Case 2, which lasted for 1.7 h, was conducted for simulating how the thermal effect influences the flow distribution of the PTSF; in this case, the DNI is maintained at 800 W/m^2 throughout the whole process. As shown in Figure 17a, the SCAs in Loop 1 will be defocused in a positive (from one to four) and a negative (from four to one) sequence. The reasons for the fluctuation of flow rate and pump pressurizing at the time of defocus are demonstrated in Case 1. As shown in Figure 17b,c, both defocus sequences cause an increase of the header flow rate and a reduction of pump pressurizing. This is because the HTF will stop expanding and has a lower velocity in the defocused SCAs compared with a focused one; this further leads to a lower pump pressure and higher pump capacity. This effect is presented in a more obvious way in the comparison of flow rate among the three loops shown in Figure 17b; the flow rate in the defocused Loop 1 increases step-by-step compared with the other two focused loops due to its lower pressure drop. Besides, compared with the negative defocused sequence, the cold HTF will flow over longer distances when the SCAs are defocused in a positive sequence. As a result, the higher flow rate and lower pump pressure exist in the positive defocused sequence due to the lower flow resistance. Finally, the HTF in the SCAs, which is closer to

the inlet, has greater thermal inertia than the SCAs near the outlet; this causes the difference of outlet temperature between the two opposite sequences of defocus shown in Figure 17d.

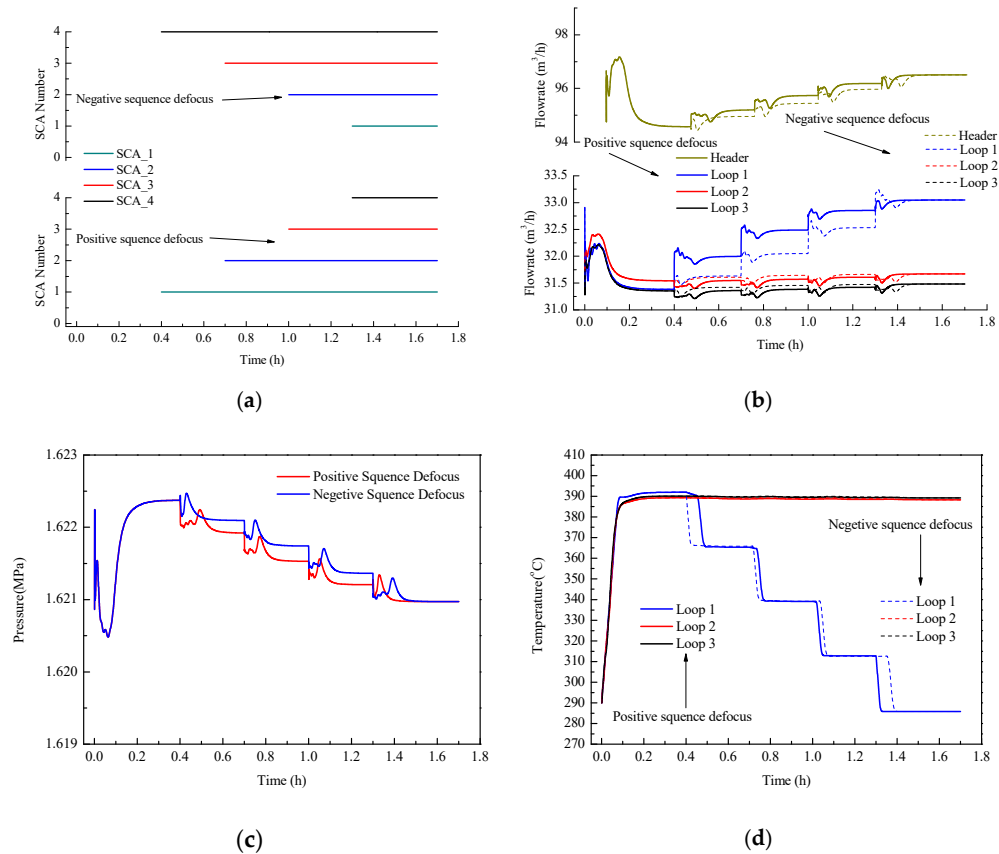


Figure 17. Simulating Case 2 for (a) initial parameters; (b) inlet flowrate results of the header and three loops; (c) pump pressurizing results; and (d) outlet temperature results of three loops.

The density, specific heat capacity, and the viscosity are the most relevant properties to the thermal hydraulic characteristics of the PTSF. Based on the simulation results of the above two cases, it can be found that when the inlet temperature of the header stays the same, the effect of density is the most influential property, followed by the specific heat capacity and viscosity. From a thermal perspective, although the specific heat capacity increases with the temperature, the thermal inertia decreases with the temperature because of the reduction of density. From a hydraulic perspective, although the viscosity decreases with the temperature, the pressure loss increases with the temperature because the expansion of the HTF causes a greater velocity.

5.2. Feedforward Control Strategy

An important function of the CTHM is being used for study of control strategy; two feedforward control strategies based on the CTHM are introduced in this section. In both strategies, the header inlet temperature is set at 290 °C, and opening of the HCV and the LCVs are the control variables that control the outlet temperature of the header and three loops at 390 °C.

The first strategy is studied under a uniform solar irradiance; as shown in Figure 18a, the DNI of the whole PTSF varies with a cosine disturbance from 800 W/m² to 400 W/m², of which the period is 0.2 h. Due to the uniformity of the DNI, a balanced flow distribution must be maintained for the same outlet temperature of the three loops, so the openings of the three LCVs are kept constant. The ideal flow rate under different DNI values can be calculated according to the thermal part of the CTHM, while the opening of the HCV and pump pressurizing can be solved according to the

hydraulic part of the CTHM and the calculated ideal flow rate; these results are shown in Figure 18b. The control results of the outlet temperature are shown in Figure 18c, the outlet temperatures of the three loops and header are all very close to 390 °C, and the small-range fluctuations of the outlet temperature in the three loops and headers are caused by the heat loss in the header, which varies with the flow rate.

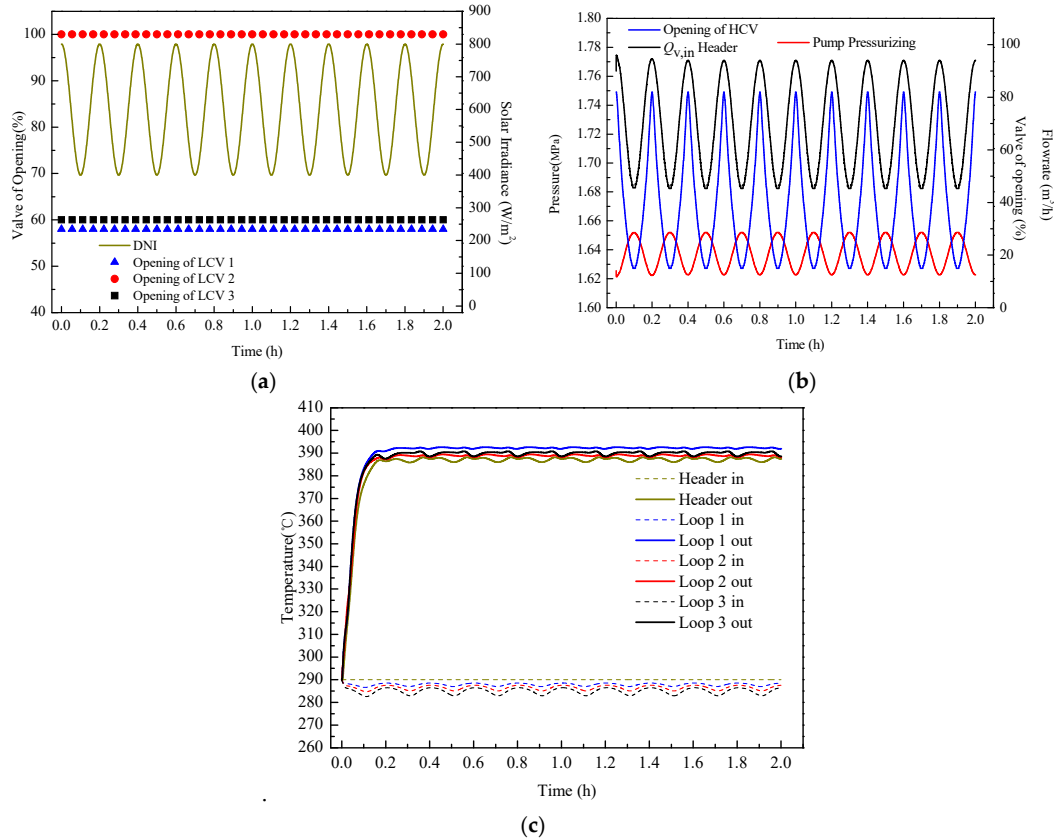


Figure 18. Header control valve (HCV) control for: (a) Initial parameters and DNI disturbance; (b) Results of HCV opening, header inlet flow rate, and pump pressurizing; (c) Results of inlet and outlet temperature of header and three loops.

The second strategy is researched under a nonuniform solar irradiance. As shown in Figure 19a, the DNI values in Loop 1 and Loop 3 are kept at 800 W/m², while for Loop 2, the DNI varied in a similar way as shown in Figure 18a. The balance of flow distribution must be thrown off due to the nonuniformity of DNI, so the opening of three LCVs should be recalculated to meet the varied DNI. The ideal flowrate distribution can also be solved by the thermal part of the CTHM, while the openings of the HCV and LCVs can be calculated in two steps. First, we set the opening of the LCV in Loop 3 at 60% and calculated the opening of the LCVs in Loop 2 and Loop 3 with the method referenced in [13] and [15]. Second, we work out the opening of the HCV and pump pressurizing by the hydraulic part of the CTHM. The above results are shown in Figure 19b: the opening of the LCVs in Loop 1 varied within a tiny scale, and the varied opening of the HCV and LCV in Loop 2 are the major variables for controlling the flow rate.

The good control results for the flow rate and outlet temperature are shown in Figure 19c,d; the key presented in the results is that the fluctuation of the header flow rate can be centered on Loop 2 if the openings of the LCV and HCV vary in a similar way. These results verify the feasibility of PTSF control by the cooperation of LCVs and HCVs under a complex distribution of DNI and SCA performance in a large-scaled plant.

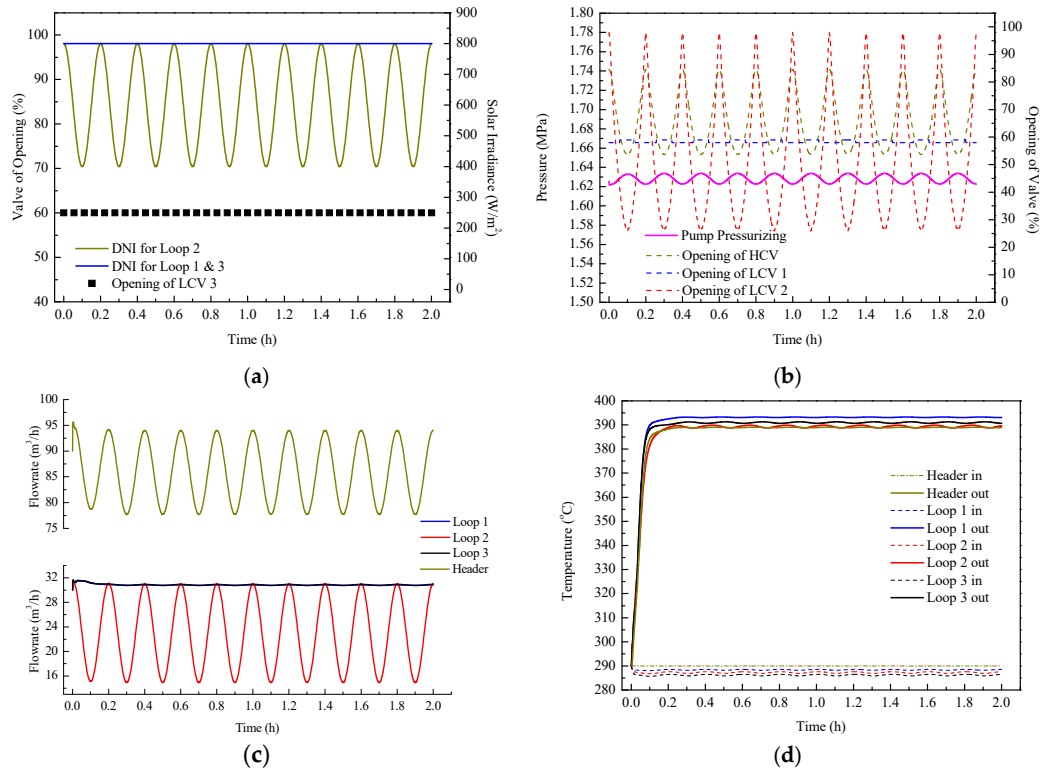


Figure 19. LCV control for (a) Initial parameters and DNI disturbance; (b) Results of HCV opening, LCV opening, and pump pressurizing; (c) Inlet flow rate results of the header and three loops; (d) Inlet and outlet temperature results of the header and three loops.

6. Conclusions

This paper mainly outlines a comprehensive thermal hydraulic model (CTHM) for the parabolic trough solar field (PTSF) based on a pilot plant. The CTHM is established and solved by a novel numerical method, validated by the experimental data based on the pilot plant, and applied to simulate the dynamic behavior and develop the control strategy of the PTSF under many types of disturbances. The main contribution of this paper is its development of a powerful model for the deeper study on PTSF. On the one hand, the total flow rate, flow distribution, pump head, and outlet temperature can be detailed and calculated by the CTHM under normal or disturbed conditions; on the other hand, when the value and distribution of the solar irradiance deviates from that of the design situation, the CTHM can also be used to calculate the opening of valves for the desired outlet temperature.

In this paper, all of work surrounds a 1 MW pilot plant, which is much smaller than a large-scaled commercial plant. However, all of the key factors (such as the unbalanced flow distribution) are included in the pilot plant, so the validity of the CTHM will always remain when it is applied to a large-scaled PTSF. In the future, the CTHM can play an important role in the further study of the commercial parabolic trough power plant, such as providing more detailed outlet parameters when combining the PTSF with a thermal storage system or power block, or using it to develop the optimal operation strategy.

Author Contributions: Conception, L.M.; methodology, L.M. and L.X.; software, L.M.; validation, L.M.; formal analysis, L.M.; investigation, L.M.; resources, L.M.; data curation, L.M.; handwriting—Original draft preparation, L.M.; handwriting—Review and editing, L.M. and D.L.; visualization, L.M.; supervision, Z.W.; project administration, Z.W. and L.X.; funding acquisition, Z.W. and L.X.

Funding: This study was supported by the National Key Research and Development Program of China (No. 2018YFB0905102).

Conflicts of Interest: We declare that we have no financial and personal relationships with other people or organizations that can inappropriately influence our work; there is no professional or other personal interest of any nature or kind in any product, service and company that could be construed as influencing the position presented in, or the review of, the manuscript entitled.

Appendix A

Table 1. Thermophysical properties of Therminol VP-1.

Property	Expression	Coefficients				
		c1	c2	c3	c4	c5
Density (kg/m ³)	$c_1T + c_2T^2 + c_3T^3 + c_4$	-0.90797	7.8116×10^{-4}	2.367×10^{-6}	1083.25	-
Kinematic viscosity (mm ² s ⁻¹)	$exp\left(\frac{c_1}{T + c_2} + c_3\right)$	544.149	114.43	-2.59578	-	-
Specific heat (J kg ⁻¹ K ⁻¹)	$c_1T + c_2T^2 + c_3T^3 + c_4T^4 + c_5$	0.002414	5.9591×10^{-6}	-2.9879×10^{-8}	4.4172×10^{-11}	1.498
Thermal conductivity (W m ⁻¹ K ⁻¹)	$c_1T + c_2T^2 + c_3T^3 + c_4T^4 + c_5$	-8.19477×10^{-5}	-1.92257×10^{-7}	2.5034×10^{-11}	-7.2974×10^{-15}	0.137743

Appendix B

In one of the iterative process, the hydraulic part can be combined to be a matrix equation of $Q_{f,in}$, $Q_{f,out}$, and p_1 ; this matrix equation can be expressed as:

$$X(Q_{f,in}^t, Q_{f,out}^t, p_1^t) = \begin{bmatrix} U_{11} & U_{12} & U_{13} \\ U_{21} & U_{22} & U_{23} \\ U_{31} & U_{32} & U_{33} \end{bmatrix} \begin{bmatrix} Q_{f,in}^t \\ Q_{f,out}^t \\ p_1^t \end{bmatrix} - \begin{bmatrix} W_1 \\ W_2 \\ W_3 \end{bmatrix} = 0 \tag{A1}$$

Where the elements of U and W are given by:

$$\begin{aligned} U_{11} &= M_{1,in}, U_{12} = M_{1,out}, U_{13} = 0 \\ U_{21} &= D(\rho_{f,in}^t), U_{22} = -D(\rho_{f,out}^t), U_{23} = 0 \\ U_{31} &= \frac{D(A_c) + D(S)D(|\bar{Q}_f^t|)}{2} - \frac{D(\rho_{f,in}^t)D(|Q_{f,in}^t|)}{D^2(A)} \end{aligned} \tag{A2}$$

$$U_{32} = \frac{D(A_c) + D(S)D(|\bar{Q}_f^t|)}{2} + \frac{D(\rho_{f,in}^t)D(|Q_{f,in}^t|)}{D^2(A)}$$

$$\begin{aligned} U_{33} &= (M_{1,in} + M_{1,out})^T \\ W_1 &= q_1^t, W_2 = D(V) \frac{(\bar{p}_f^t - \bar{p}_f)}{\Delta t} \end{aligned} \tag{A3}$$

$$W_3 = (M_{0,in} + M_{0,out})^T p_0^t + D(B_c)\bar{Q}_f$$

X is a system of nonlinear equations; these kinds of equations are frequently solved by the Newton–Raphson iterative method, which can be shown as [17]:

$$J(x^{(m)})(x^{(m+1)} - x^{(m)}) = -F(x^{(m)}) \tag{A4}$$

where J is the jacobian matrix of $F(x)$ and m is the iteration number.

Before calculating the jacobian matrix, the partial of the pressure loss and pump head with respect to $\mathbf{Q}_{f,in}$, $\mathbf{Q}_{f,out}$ must be introduced. The partials can be given by [29]:

$$\begin{aligned} P_{in} &= \frac{\partial \left(D(S) D(|\bar{\mathbf{Q}}_f|) \bar{\mathbf{Q}}_f - D(\rho_f) g H \right)}{\partial \mathbf{Q}_{in}} \\ &= \frac{\partial S_p}{\partial \mathbf{Q}_{in}} D(|\bar{\mathbf{Q}}_f|) D(\bar{\mathbf{Q}}_f) + D(S) D(|\bar{\mathbf{Q}}_f|) - D(\rho_f) g \frac{\partial H}{\partial \mathbf{Q}_{in}} \\ \frac{\partial S_p}{\partial \mathbf{Q}_{in}} &= \frac{\partial S_p}{\partial f} \frac{\partial f}{\partial Re} \frac{\partial Re}{\partial \mathbf{Q}_{in}} \\ P_{out} &= \frac{\partial S_p}{\partial \mathbf{Q}_{out}} D(|\bar{\mathbf{Q}}_f|) D(\bar{\mathbf{Q}}_f) + D(S) D(|\bar{\mathbf{Q}}_f|) - D(\rho_f) g \frac{\partial H}{\partial \mathbf{Q}_{in}} \end{aligned} \quad (A5)$$

where S_p , f , and Re are the vectors of pipe resistance, inner friction factor, and Reynolds number, respectively.

According to Equation (A4), the $(m+1)$ th iterative calculation of function X can be expressed as:

$$\begin{bmatrix} Y_{11} & Y_{12} & Y_{13} \\ Y_{21} & Y_{22} & Y_{23} \\ Y_{31} & Y_{32} & Y_{33} \end{bmatrix} \begin{bmatrix} \mathbf{Q}_{f,in}^{(m+1)} \\ \mathbf{Q}_{f,out}^{(m+1)} \\ \mathbf{p}_1^{(m+1)} \end{bmatrix} - \begin{bmatrix} \mathbf{Z}_1 \\ \mathbf{Z}_2 \\ \mathbf{Z}_3 \end{bmatrix} = \mathbf{0} \quad (A6)$$

where the elements Y and Z are given by:

$$Y_{11} = \mathbf{M}_{1,in}, Y_{12} = \mathbf{M}_{1,out}, Y_{13} = \mathbf{0}, Y_{21} = D(\rho_{f,in}^t), Y_{22} = -D(\rho_{f,out}^t), Y_{23} = \mathbf{0}$$

$$Y_{31} = \frac{D(A_c)}{2} - \frac{2D(\rho_{f,in}^t)D(|\mathbf{Q}_{f,in}^{(m)}|)}{D^2(A)} + \mathbf{P}_{in}^{(m)} \quad (A7)$$

$$Y_{32} = \frac{D(A_c)}{2} + \frac{2D(\rho_{f,out}^t)D(|\mathbf{Q}_{f,out}^{(m)}|)}{D^2(A)} + \mathbf{P}_{out}^{(m)}$$

$$Y_{33} = (\mathbf{M}_{1,in} + \mathbf{M}_{1,out})^T$$

$$\mathbf{Z}_1 = \mathbf{q}_1^t, \mathbf{Z}_2 = D(V) \frac{(\bar{\rho}_f^t - \bar{\rho}_f)}{\Delta t}$$

$$\mathbf{Z}_3 = -X(\mathbf{Q}_{f,in}^{(m)}, \mathbf{Q}_{f,out}^{(m)}, \mathbf{p}_1^m) + \frac{D(A_c)}{2} (\mathbf{Q}_{f,in}^{(m)} + \mathbf{Q}_{f,out}^{(m)}) \quad (A8)$$

$$+ \left(-\frac{2D(\rho_{f,in}^t)D(|\mathbf{Q}_{f,in}^{(m)}|)}{D^2(A)} + \mathbf{P}_{in}^m \right) \mathbf{Q}_{f,in}^{(m)} + \left(\frac{2D(\rho_{f,out}^t)D(|\mathbf{Q}_{f,out}^{(m)}|)}{D^2(A)} + \mathbf{P}_{out}^m \right) \mathbf{Q}_{f,out}^{(m)}$$

Finally, the solution of the hydraulic model can be shown as:

$$\mathbf{p}_1^{(m+1)} = \mathbf{E}_c^{-1} \left(\mathbf{M}_{1,out} (\rho_{f,out}^t)^{-1} \mathbf{Z}_2 + \mathbf{q}_1^t - (\mathbf{M}_{1,in} + \mathbf{M}_{1,out} D^{-1}(\rho_{f,out}^t) D(\rho_{f,in}^t)) \mathbf{C}_c^{-1} \right)$$

$$\mathbf{Q}_{f,in}^{(m+1)} = \mathbf{C}_c^{-1} \left(\mathbf{D}_c + (\mathbf{M}_{1,in} + \mathbf{M}_{1,out})^T \right) \mathbf{p}_1^{(m+1)} \quad (A9)$$

$$\mathbf{Q}_{f,out}^{(m+1)} = D^{-1}(\rho_{f,out}^t) \left(D(\rho_{f,in}^t) \mathbf{Q}_{f,in}^{(m+1)} - \mathbf{Z}_2 \right)$$

The whole expression of \mathbf{C}_c , \mathbf{D}_c , and \mathbf{E}_c is given by:

$$\begin{aligned}
 \mathbf{C}_c &= \mathbf{Y}_{31} + \mathbf{Y}_{32} \mathbf{D}^{-1}(\rho_{f,out}^t) \mathbf{D}(\rho_{f,in}^t) \\
 \mathbf{D}_c &= \mathbf{Z}_3 + \mathbf{Y}_{32} \mathbf{D}^{-1}(\rho_{f,out}^t) \mathbf{Z}_2 \\
 \mathbf{E}_c &= (\mathbf{M}_{1,in} + \mathbf{M}_{1,out} \mathbf{D}^{-1}(\rho_{f,out}^t) \mathbf{D}(\rho_{f,in}^t)) \mathbf{C}_c^{-1} (\mathbf{M}_{1,in} + \mathbf{M}_{1,out})^T
 \end{aligned}
 \tag{A10}$$

It is noteworthy that E_c will degrade into a definite matrix when $\rho_{f,in} = \rho_{f,out}$; i.e., the hydraulic model is not affected by the temperature, and this conclusion is consistent with [18].

Nomenclature

Latin symbols:

A/A	Area (m ²)/Area vector
b	Pipe number
B	Constant
B, C, D, E, U, W, Y, Z	Coefficient matrix
c	Specific heat capacity (J kg ⁻¹ K ⁻¹)
D	Diameter (m)
f	Friction factor or optical efficiency factor
F	Flow loss (MPa)
G	Flow coefficient
h	Convection heat transfer coefficient (W m ⁻² K ⁻¹)
H/H	Heat (W m ⁻¹) or pump head (m)/pump header vector
I	Direct normal irradiance (W m ⁻²)
k	Thermal conductivity (W m ⁻¹ K ⁻¹)
K	Pressure drop coefficient
l/l	Length (m)/Length vector
M	Incidence matrix
n	Node number
Nu	Nusselt number
op	Opening of valve
P	Power flux (W m ⁻¹)
p/p	Pressure (bar)/Pressure vector
P	Partial vector
Pr	Prandtl number
Q/Q	Volume flowrate (m ³ /h)/Volume flowrate vector
q	Node volume flowrate vector (m ³ /h)
R	Valve adjustable ratio
Re/Re	Reynolds number/Reynolds number vector
r	Mirror reflectivity
S/S	Flow resistance/Flow resistance vector
t	Time (s)
T	Temperature (°C)
V	Volume vector
W	Width (m)

Greek:

α	Absorbance
β	Defocused factor
γ	Intercept factor
δ	Thickness (m)
ε	Absolute roughness
η	Efficiency
θ	Incidence angle (°)
κ	Incidence angle modifier
ρ/ρ	Density (kg m ⁻³)/Density vector
τ	Transmittance
ω	Zenith angle (°)

Subscripts:

abs	Absorber tube
cl	Clean mirror
col	Collecto
end	End loss
f	Fluid
fit	Pipe fitting
fl	Focal distance
ins	Insulated pipe
l	Heat loss
max	Max
o	Optical
P	Pipe
rs	Row spacing
sha	Shadowing
va	Valve
use	Useful
Superscript:	
i,j	Element number of the matrix
m	iterations
t	Time layer number
Abbreviations:	
CTHM	Comprehensive thermal hydraulic model
DNI	Direct Normal Irradiance
HCV	Header control valve
HTF	Heat Transfer Fluid
LCV	Loop control valve
PTC	Parabolic trough collector
PTSTPP	Parabolic trough solar thermal power plant
PTSF	Parabolic trough solar field
SCA	Solar collector assembly
THDM	Thermal hydraulic dynamic model

References

1. Yilmaz, I.H.; Mwesigye, A. Modeling, simulation and performance analysis of parabolic trough solar collectors: A comprehensive review. *Appl. Energy* 2018, *225*, 135–174.
2. Cheng, Z.-D.; He, Y.-L.; Wang, K.; Du, B.-C.; Cui, F. A detailed parameter study on the comprehensive characteristics and performance of a parabolic trough solar collector system. *Appl. Therm. Eng.* 2014, *63*, 278–289.
3. Giotri, A. Transient Effects in Linear Concentrating Solar Thermal Power Plant. Ph.D. Thesis, Polytechnic University of Milan, Milan, Italy, 2014.
4. Forristall, R. *Heat Transfer Analysis and Modeling of a Parabolic Trough Solar Receiver Implemented in Engineering Equation Solver*; Technical Report NREL/TP-550-34169; National Renewable Energy Laboratory: Golden, CO, USA, 2003.
5. Dudley, V.E.; Kolb, G.J.; Mahoney, A.R.; Mancini, T.R.; Matthews, C.W.; Sloan, M.; Kearney, D.W. *Test Results: SEGS LS-2 Solar Collector*; Nasa Sti/recon Technical Report N; Sandia National Labs.: Albuquerque, NM, USA, 1994; p. 96.
6. Stuetzle, T.; Blair, N.; Mitchell, J.W.; Beckman, W.A. Automatic control of a 30 MWe SEGS VI parabolic trough plant. *Sol. Energy* 2004, *76*, 187–193.
7. Camacho, E.F.; Berenguel, M. Control of solar energy systems. *IFAC Proc. Vol.* 2012, *45*, 848–855.
8. Padilla, R.V.; Demirkaya, G.; Goswami, D.Y.; Stefanakos, E.; Rahman, M.M. Heat transfer analysis of parabolic trough solar receiver. *Appl. Energy* 2011, *88*, 5097–5110.
9. Hachicha, A.; Rodríguez, I.; Capdevila, R.; Oliva, A. Heat transfer analysis and numerical simulation of a parabolic trough solar collector. *Appl. Energy* 2013, *111*, 581–592.
10. Yilmaz, I.H.; Söylemez, M.S. Thermo-mathematical modeling of parabolic trough collector. *Energy Convers. Manag.* 2014, *88*, 768–784.

11. Behar, O.; Khellaf, A.; Mohammedi, K. A novel parabolic trough solar collector model—Validation with experimental data and comparison to Engineering Equation Solver (EES). *Energy Convers. Manag.* 2015, *106*, 268–281.
12. Wagner, M.J.; Gilman, P. *Technical Manual for the SAM Physical Trough Model*; National Renewable Energy Laboratory: Golden, CO, USA, 2011.
13. Abutayeh, M.; Alazzam, A.; El-Khasawneh, B. Balancing heat transfer fluid flow in solar fields. *Sol. Energy* 2014, *105*, 381–389.
14. Noureldin, K.; Hirsch, T.; Pitz-Paal, R. Virtual Solar Field—Validation of a detailed transient simulation tool for line focus STE fields with single phase heat transfer fluid. *Sol. Energy* 2017, *146*, 131–140.
15. Ma, L.; Xu, E.; Li, J.; Xu, L.; Li, X. Analysis and validation of a thermal hydraulic dynamic model for the parabolic trough solar field. *Energy* 2018, *156*, 430–443.
16. Todini, E.; Pilati, S. A gradient method for the solution of looped pipe networks. In *Computer Applications in Water Supply*; Research Studies Press: Taunton, UK, 1988; Volume 1, pp. 1–20.
17. Ellis, D.J. The Behaviour of Pipe Network Analysis Solution Techniques. Ph.D. Thesis, University of Adelaide, Adelaide, Australia, 2001.
18. Nault, J.D.; Karney, B.W. Improved Rigid Water Column Formulation for Simulating Slow Transients and Controlled Operations. *J. Hydraul. Eng.* 2016, *142*, 04016025.
19. Colmenar-Santos, A.; Munuera-Pérez, F.-J.; Tawfik, M.; Castro-Gil, M. A simple method for studying the effect of scattering of the performance parameters of Parabolic Trough Collectors on the control of a solar field. *Sol. Energy* 2014, *99*, 215–230.
20. Almasabi, A.; Alobaidli, A.; Zhang, T.; Zhang, T. Transient Characterization of Multiple Parabolic Trough Collector Loops in a 100 MW CSP Plant for Solar Energy Harvesting. *Energy Procedia* 2015, *69*, 24–33.
21. Padilla, R.V. Simplified Methodology for Designing Parabolic trough Solar Power Plants. Ph.D. Thesis, University of South Florida, Tampa, FL, USA, 2011.
22. Karassik, I.J.; Messina, J.P.; Cooper, P.; Heald, C.C. *Pump Handbook*, 3rd ed.; McGraw-Hill: New York, NY, USA, 2001; p. 2.70.
23. Arias, D.A.; Gavilán, A.; Russel, M. Pumping Power Parasitics in Parabolic Trough Solar Fields. In Proceedings of the 15th International SolarPACES Symposium, Berlin, Germany, 15–18 September 2009.
24. Skousen, P.L. *Valve Handbook*, 1st ed.; McGraw-Hill: New York, NY, USA, 1997; pp. 24–33.
25. Chaudhry, M.H. *Applied Hydraulic Transients*, 3rd ed.; Van Nostrand Reinhold: New York, NY, USA, 2014; pp. 35–43.
26. Munson, B.R.; Young, D.F.; Okiishi, T.H. *Fundamentals of Fluid Mechanics*, 6th ed.; John Wiley & Sons. Inc.: New York, NY, USA, 2009; pp. 411–412.
27. Churchill, S.W. Friction-factor equation spans all fluid-flow regimes. *Chem. Eng.* 1977, *84*, 91–92.
28. Zhao, D.; Xu, E.; Wang, Z.; Yu, Q.; Xu, L.; Zhu, L. Influences of installation and tracking errors on the optical performance of a solar parabolic trough collector. *Renew. Energy* 2016, *94*, 197–212.
29. Simpson, A.; Elhay, S. Jacobian Matrix for Solving Water Distribution System Equations with the Darcy-Weisbach Head-Loss Model. *J. Hydraul. Eng.* 2011, *137*, 696–700.

